

Two-dimensional imaging velocity interferometry: Data analysis techniques

David J. Erskine,^{1,a)} R. F. Smith,¹ C. A. Bolme,² P. M. Celliers,¹ and G. W. Collins¹

¹Lawrence Livermore National Laboratory, P.O. Box 808, Livermore, California 94551, USA

²Los Alamos National Laboratory, Los Alamos, New Mexico 87545, USA

(Received 5 November 2011; accepted 4 April 2012; published online 27 April 2012)

We describe data analysis procedures for an emerging interferometric technique for measuring target motion across a two-dimensional image at a moment in time, i.e., a snapshot 2D-VISAR. Conventional VISARs (velocity interferometer system for any reflector) are commonly used in shock physics to measure velocity history at a single point or many points across a line on target. These however are not recorded in two-dimensions and cannot be used with ultrashort pulsed illumination because the coherence length is smaller than the interferometer delay, preventing fringe formation. In our scheme, dual matched interferometers allow use of low- or incoherent illumination such as ultrashort laser pulses to freeze motion of target, allowing use of slow CCD imaging detectors. Quadrature phase recording and push-pull data analysis simultaneously produces an ordinary nonfringing reflectivity image and a fringing image. The latter is converted into a 2D-phase map which is proportional to target velocity. Example data on shocked crystalline [111] Si shows incipient features of $\sim 50 \mu\text{m}$ scale. © 2012 American Institute of Physics. [<http://dx.doi.org/10.1063/1.4704840>]

I. INTRODUCTION

An important diagnostic for shock physics over many years has been a velocity interferometer system for any reflector (VISAR),¹⁻⁴ which measures target motion to high precision. Until recently, this diagnostic has been limited to measuring motion at points or lines across a target. We introduce an emerging interferometric technique for measuring motion across a two-dimensional image, which could be called a snapshot 2D-VISAR.

A conventional VISAR is usually an imaging system (that imprints fringes on the target image which shift in phase in response to target motion). In principle a fast movie camera could be placed behind a traditional VISAR and records the history of the 2D fringing image. (Actually, four images need to be recorded, one for each of the quadrature outputs.) Framing camera technology with 1–5 ns exposure times are commercially available. However, in shock physics experiments time-dependent material deformation processes such as structural phase transformations or fracture can occur over nanosecond or less timescales. Therefore imaging these phenomena without significant motion blurring requires a diagnostic with sub-nanosecond resolution. Rather than use ns-scale framing cameras to record a movie of several frames, we use instead an inexpensive 4000×4000 pixel CCD detector, and record only a single moment in time, using the brevity of picosecond pulsed laser illumination to provide the time resolution.

However, the coherence length of our illumination (~ 3 ps) is much shorter than the VISAR interferometer delay (~ 300 ps), which is the pathlength difference between the two arms. This would prevent fringes from forming in the output of a conventional (single interferometer) VISAR. Without fringes, the VISAR cannot work.

We solve this problem by using the white light velocimetry configuration⁵⁻⁹ (Fig. 1). In this scheme, two interferometers (illuminating, detecting) having nearly identical delays are used in series, with one before the target and one after. This produces fringes with at most 50% visibility, but otherwise has the same fringe shift per target motion behavior of a traditional VISAR. That is, the same data analysis schemes (including the one described in this paper) will work for either conventional or short pulse VISAR.

The 2D-VISAR provides a valuable new kind of information about shock behavior not readily accessible by traditional point or 1D-VISARS, simultaneously providing both a 2D velocity map and an ordinary reflectivity snapshot image of the target. Consider the trigonal symmetry easily seen in an emerging spherical shock from [111] single crystalline Si (Fig. 2), in raw data. This kind of observation is not readily accessible by point or line VISARs because they are too expensive to field in multiple quantities. The 2D-VISAR has been used to observe shock front nonuniformities in National Ignition Facility related targets (polycrystalline diamond, Be),^{10,11} and in Si and Al.

The focus of this paper is to describe the data analysis procedures, including push-pull analysis to process quadrature data into phase maps, how to judge optimal push-pull parameters, and the Fourier analysis that takes advantage of the 2D nature of the data.

A. Target information for example shot

Figure 3 shows the target geometry for the example shot 020910-04 used in the figures below. Details of the interferometer optics can be found in Ref. 7. The example experiment observes a pressure wave leaving a silicon free surface. One beam of the (Janus) laser at 527 nm delivered 236 J in a 6 ns square pulse onto the CH/Al/Si target, which generated an ablatively driven planar shock. A kinoform phase plate

^{a)}Electronic mail: erskine1@llnl.gov.

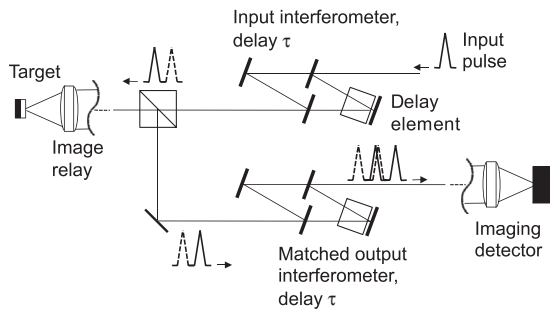


FIG. 1. The white light or short pulse velocimeter scheme, which uses matched-delay illuminating and detecting interferometers, is a method of producing partial (50%) visibility fringes in spite of the laser pulsewidth being shorter than the interferometer delay. Otherwise, no visible fringes would result. The inner two pulses of the outputted four overlap, producing fringes.

inserted into the beam produced a 1 mm square drive spot, with $\sim 5\%$ intensity uniformity at the focal plane. The $10\ \mu\text{m}$ CH ablative layer was directed deposited onto the Al. Using a hydrocode the peak shock pressure launched into the Al was estimated to be ~ 70 GPa. The single-crystal silicon layer was $300\ \mu\text{m}$ thick and had [111] orientation in the pressure loading direction. Image scaling is $0.53\ \mu\text{m}$ on target per pixel.

B. Companion line-VISAR

In addition to the 2D-VISAR which takes a snapshot measurement, we also simultaneously measure the target with a Line-VISAR which measures velocity vs time along a slit imaged across the middle of the sample (box in right image of Fig. 4). For the example shot the brief 2D-VISAR probe illumination occurs immediately after shock arrival. The velocity from the Line-VISAR can help resolve some fringe skip ambiguities in the 2D-VISAR measurement in general, although it is not needed for the particular example shot, since the rise of velocity at the edge of the drive region is clearly resolved without loss of fringe contrast.

C. 2D-VISAR

Figure 5 shows the raw image from CCD detector which records the four quadrature interferometer outputs. The edge

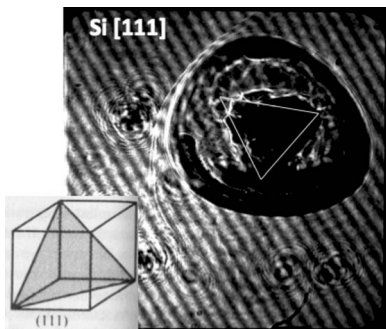


FIG. 2. Trigonal symmetry of a spherical shock wave emerging from 1 mm thick Si along the [111] direction is immediately apparent with an 2D-imaging VISAR. The 2D-VISAR allows a valuable new kind of data not accessible by point or line-VISARs. Field of view ~ 3 mm for this shot 081209-04. This is a raw exposure having fringes.

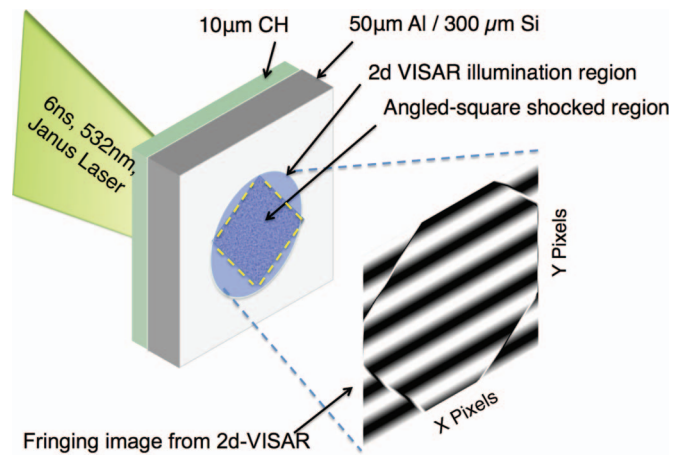


FIG. 3. The 2D-VISAR target geometry for the example shot 020910-04. Laser pulse delivers 236 J onto a 1 mm square region of CH layer which generates a planar shock into 50 μm Al, then 300 μm single crystal Si at [111] orientation. This breaks out into vacuum where it is observed by 2D-VISAR (illuminated by a circular beam but recorded by a square detector region). The VISAR interferometer imposes fringes of four different phases and records these on four quadrants of one detector.

of the tilted square drive laser spot can be seen. The round 2D VISAR probe beam covers both driven and undriven regions.

The bias fringes created by slightly tilting an interferometer mirror are apparent. The right pair have complementary phase; similarly for left pair. Left and right pairs ideally differ in phase by 90° , but for this and many recent shots actually differ by about 60° . (This nonquadrature is compensated by the obliquity transformation, Sec. II B.)

1. Initial data processing steps

Split into quadrants. The raw 4096×4096 pixel image from the CCD detector (Fig. 5) is split into four quadrants of 2000×2000 size, to overlay each other. The channel numbers are labeled, clockwise starting at upper right, 0, 2, 3, 1.

Precision Overlay. One quadrant is designated the home quadrant. Each of the other three quadrants are compared to the home quadrant. For each pair, four small sections in a north, south, east, west arrangement of each quadrant are correlated to find detailed values for rotation, translation, and magnification. The result of these transformations is a stack of 2000×2000 images having four intensities $S_n(x, y)$ per pixel. The correlation peak width can be as small as ~ 3 –5 pixels, indicating focus quality. Correlations usually can be done on the shot exposure (preferred)—if not, then on the reference exposure made prior to the shot.

II. EQUATIONS FOR FINDING FRINGE PHASE

The interferometer output for the channels n is

$$S_n(x, y) = I(x, y)\{1 + \gamma \cos 2\pi[\theta(x, y) + \phi_n]\} + C_n, \quad (1)$$

where the fringe visibility γ has a maximum value of 0.5 due to the partial coherence of the white light velocimetry arrangement. The γ decreases from 0.5 by interferometer misalignment, target surface quality under shock loading, or

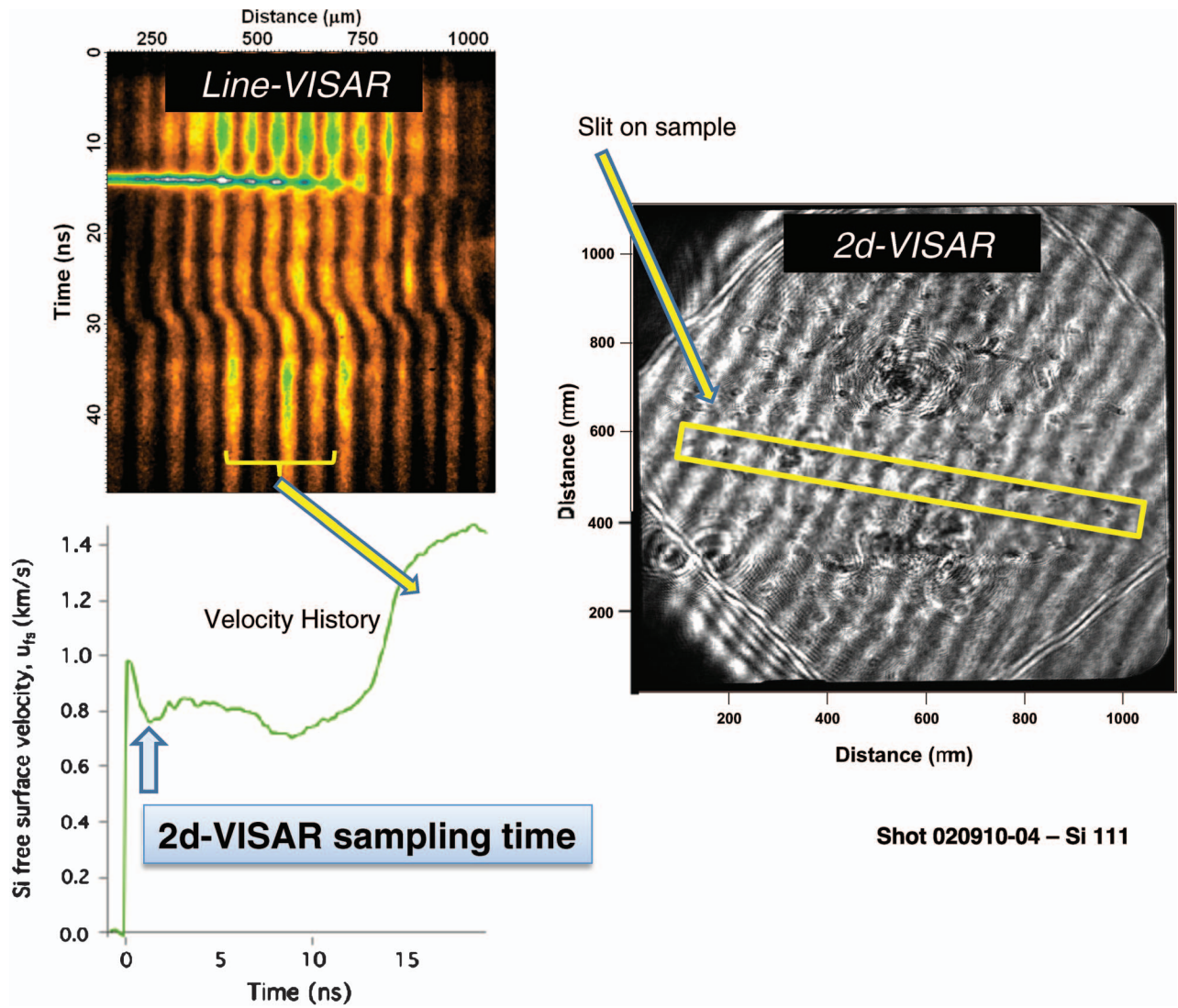


FIG. 4. Line-VISAR interferogram (upper left) measures the target velocity history (bottom left) at the linear location on the 2D target image (right) indicated by the box “Slit on sample,” through the middle of target area. Zero time of the velocity history is set to moment of shock arrival at the Si-vacuum free surface. In our experimental setup the 2D sampling time can be set arbitrarily relative to the shock arrival time to within an accuracy of less than 50 ps. For the shot shown here the 2D sampling moment was $t_0 + 1.33$ ns. The bright horizontal feature at ~ 14 ns in the Line-VISAR interferogram is a timing mark near this moment.

phase nonquadrature. The four output channel phases ϕ_n are ideally in 90° intervals, but often irregular by $\sim 30^\circ$. This irregularity is tolerated by the push-pull math. The target reflected intensity is $I(x, y)$ and detected intensity $S(x, y)$. The $\theta(x, y)$ is the fringe phase we seek, which describes displacement of target surface during interferometer delay interval τ .

The C_n in Eq. (1) represents any incoherent contribution that has a different spatial dependence than $I(x, y)$, which could be target chamber blackbody light, or detector bias current. These will usually be much smaller level than I and will mostly cancel in the push-pull math.

A. Push-pull equations

The push-pull equations below combine the four detected signals S_n into fringing F and nonfringing I outputs. These

equations are applied to each pixel (as if we had a single point VISAR), and thus we can omit the (x, y) . These are similar to those of Hemsing² except for the way we handle the non-quadrature issue. The first balancing equations use adjustable gains g_{02} , g_{hv} , etc.

$$S'_0 = g_{hv}(g_{02}S_0 + h_0), \quad (2)$$

$$S'_1 = (g_{13}S_1 + v_0), \quad (3)$$

$$S'_2 = g_{hv}S_2, \quad (4)$$

$$S'_3 = S_3, \quad (5)$$

where the subscripts refer to channel numbers or pairs of channels (h for 0 and 2; v for 1 and 3). These are then

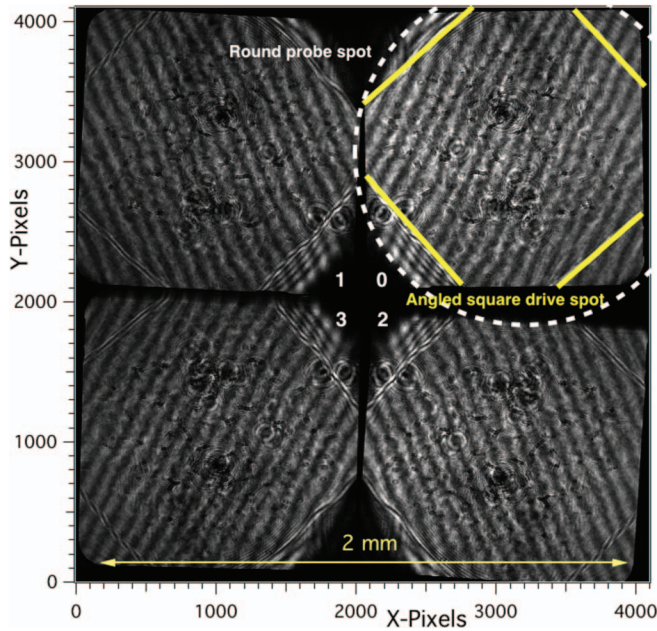


FIG. 5. Raw 4096×4096 image from CCD detector records four quadrature interferometer outputs, labeled 0–3 at the center. The drive laser spot is square and angled relative to detector. The round 2D VISAR probe beam covers both driven and undriven regions. The bias fringes can be seen. The right pair (0, 2) have complementary phase; similarly for left pair (1, 3). Left and right pairs differ in phase by about 60° (ideally 90°).

combined via

$$I = (S'_0 + S'_1 + S'_2 + S'_3)/4, \quad (6)$$

$$F = (S'_0 - S'_2)/2 + i(S'_1 - S'_3)/2, \quad (7)$$

to form the nonfringing intensity I and the complex fringing field F . The former combines terms to cancel the fringes. The latter subtracts terms to reveal the fringing component.

The F is complex and to visualize its behavior we plot it as a Lissajous in the complex plane, $\Im F$ vs $\Re F$ (Fig. 6(a)), imaginary vs real parts. Since this requires an extra dimension to show the imaginary, it is only practical to make a 2D-Lissajous plot of a 1D-strip, not 2D-region of data from F . We call it a “lineout,” although it could be along any convenient path.

B. Obliquity: Correcting nonquadrature

The obliquity transform compensates for nonquadrature. As the phase intervals become non-ideal, the “vertical” complementary channels (S_0, S_2) and “horizontal” complementary channels (S_1, S_3) become more correlated, which causes the Lissajous to become more elliptical along an axis at 45° to the regular axes. Thus one can compensate by distorting the Lissajous along a new coordinate system, at 45° to the original, via an obliquity parameter g_q , nominally unity. This transformation is

$$u = \Re F + \Im F; \quad v = \Re F - \Im F, \quad (8)$$

$$u \leftarrow u * g_q, \quad (9)$$

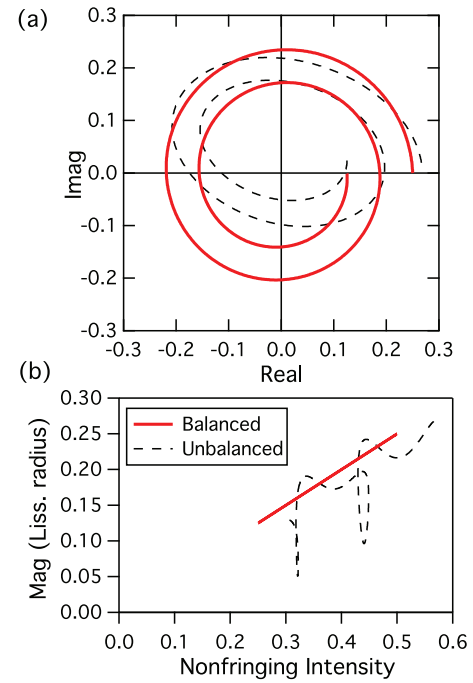


FIG. 6. The effect of non-optimal gain parameters is shown on simulated data. Optimal parameters (solid curve) produce the most circular Lissajous, $\Im F$ vs $\Re F$ (top), and most linear magnitude $|F|$ vs intensity I (bottom). Non-optimal parameters produce dashed curves.

$$\Re F' = (u + v)/2; \quad \Im F' = (u - v)/2, \quad (10)$$

$$F = \Re F' + i \Im F'. \quad (11)$$

Typically we see g_q range ~ 0.6 – 1.7 .

C. Optimizing push-pull gains

The optimal push-pull and obliquity gains and offsets are found by analyzing several representative 1D-lineouts of the 2D-data, (1D so that a Lissajous can be displayed). Once optimal gains are found for each region, one decides whether it is necessary to subdivide the image into smaller regions each having its own set of gains, or to use one set for the entire image. Then the equations with these gains are applied to all the pixels of the 2D-data.

The 1D-lineout is best taken approximately perpendicular to the bias fringes, and with at least one period (~ 100 pixels) of phase range. Then using Eqs. (2)–(11), a Lissajous plot of $\Im F$ vs $\Re F$ is made and all gains and offsets are adjusted until the Lissajous is centered and circular.

For a point on the Lissajous path, the angle corresponds to target velocity and radius (magnitude) from origin corresponds to fringe visibility which is affected by intensity. Blurring effects tend to reduce fringe visibility which causes the path to head toward the origin. Low intensity, such as due to laser speckle, will also reduce Lissajous magnitude. When the path is near the origin, it is especially sensitive to noise offsets that push it to the wrong side of the origin, changing the phase (in cycles) by an integer, creating a fringe skip problem in θ

(Sec. III C). Thus it is important that the Lissajous is properly centered, particularly for the low intensity areas.

1. Adjustable gains effects

The adjustable gains have the following effects: the offsets h_0 , v_0 , translate the Lissajous ($\Im F$ vs $\Re F$) and corrects for any C_n which survives cancellation between complementary channel pairs. The horizontal to vertical astigmatism g_{hv} stretches the Lissajous along x or y axes. The obliquity g_q stretches the Lissajous along an axis 45° to the regular axes.

The left/right asymmetry g_{02} and up/down asymmetry g_{13} translate the larger radius portions of the Lissajous relative to the smaller radius portions, as if the data were a cylinder emerging from the page and the end near you was being moved. (For data that have a constant magnitude $|F|$, these are not used since their effects are degenerate with offsets h_0 , v_0 .) We recommend first using h_0 , v_0 to center the inner radius portions of the Lissajous, and then use g_{02} and g_{13} to center the outer portions.

2. Additional diagnostics

An additional diagnostic is to plot magnitude vs intensity and adjust gains and offsets for maximum linearity (Fig. 6(b) and Sec. III B). This is needed especially when the lineout is short so the Lissajous only makes a few circuits. Then it may be legitimately noncircular due to intensity (and thus magnitude) changes, which can confuse the location of the proper center.

Another indication of non-optimal gains is the appearance of the bias fringe periodicity or its 2nd harmonic in the Fourier transform of $I(x, y)$, or the 2nd harmonic in $F(x, y)$.

In addition to the four-channel intensity Eq. (6), it is useful to also compute separate horizontal and vertical intensities

$$I_h = (S'_0 + S'_2)/2, \quad (12)$$

$$I_v = (S'_1 + S'_3)/2. \quad (13)$$

If these have a dissimilar shape then the four channels are inconsistent and at least one may be bad. It is possible to discard a bad channel and substitute faux data, reconstructed by assuming $I_h \propto I_v$.

D. Computing outputs for all pixels

After finding optimal gains and offsets, one applies Eqs. (2)–(11) to all pixels. The fundamental outputs are the nonfringing intensity $I(x, y)$, which is essentially an ordinary reflectivity snapshot image of the target, and the complex fringing function $F(x, y)$ which embodies target motion through $\theta(x, y)$. We can express $F = |F|e^{i2\pi\theta}$ and obtain the magnitude $|F|$ and phase θ via

$$|F|^2 = (\Im F)^2 + (\Re F)^2, \quad (14)$$

$$\tan 2\pi\theta = \frac{\Im F}{\Re F}. \quad (15)$$

E. Removal of bias phase slope

The bias phase slope can be conveniently removed via Fourier transform (FFT) of F , since it translates the transform by an amount easily recognized by a spike in the FFT. One may postpone this step until after the unwrapping.

F. Phase unwrapping

The phase is unwrapped to eliminate its periodic nature, hopefully eliminating all fringe skips. We use a library function *ImageUnwrapPhase* by Wavemetrics, Inc. based on an algorithm described in Ref. 12. In 1D this is simple, but in 2D when it encounters a spiral type of phase irregularity called a ‘‘pole’’ which it may not be able to remove.

G. Repair of occasional phase ambiguity

The phase ambiguities which are not fixed by the unwrapping are fixed by substituting either blurred or modeled proxy data. (The blurred proxy requires the unwrapping to be attempted at least once.) Then the unwrapping process is re-applied. Details are described in Sec. III C.

H. Phase to velocity proportionality

The fringe phase $\theta(x, y)$ in cycles describes the change in target displacement, in distance units of wavelength λ , over an interval of time τ , which is the detecting interferometer delay (pathlength difference between arms). In most cases this can be interpreted as a velocity which is proportional to θ by a velocity per fringe (VPF) constant. The VPF is set by the delay ($\tau = 268.5$ ps) expressed in time units, through¹³

$$\text{VPF} = \frac{\lambda}{2\tau(1 + \delta)}, \quad (16)$$

where the probe wavelength λ is 400 nm, $\delta = 0.05678$ is a dispersion correction factor for the fused silica glass etalon used to create the delay, and the factor of 2 is due to the roundtrip geometry between target and interferometers. The VPF for the example data is 705 m/s per fringe. We now have a velocity map $V(x, y) = \text{VPF}\theta(x, y)$.

An optional step is to perform a similar analysis on the reference exposure taken of the stationary target, and subtract its phase map from the shot phase map. This will help reduce ring-like artifacts produced by dust specks on the optics. This concludes the push-pull analysis of the data.

I. Fourier analysis

It is useful to study the roughness character of different parts of a shocked surface by taking a 2D-FFT of the phase map $\theta(x, y)$. The growth of instabilities in the shock front can be studied, and this growth rate can depend on spatial frequency. Targets constructed with a periodic ripple in their surface have been studied using a 2D-VISAR at Rochester’s

Omega laser facility.^{7,10,11} This information is valuable for predicting behavior of shock front instabilities in laser fusion targets at the National Ignition Facility.

While the principal interest is in the FFT of θ , one can also study the FFT of $I(x, y)$, $F(x, y)$ or $F/|F|$. The interesting advantage of the latter two is that they are immune to phase ambiguities, since the phase is periodic inside F anyways. For small θ , the $e^{i2\pi\theta} \approx 1 + 2\pi\theta$, so the FFT of $F/|F|$ approximates the FFT of θ for all but the lowest frequencies where θ fluctuations tends to be larger.

III. DISCUSSION OF PUSH-PULL STRATEGY

A. Correction of nonquadrature

We handle the nonquadrature issue in a different manner than Hemsing.² He uses $\tan 2\pi\theta = \frac{\Im F}{\sin \beta \Re F} - \cot \beta$, with a parameter β which is the phase between quadrature coded signals. We choose to simplify the equation to $\tan 2\pi\theta = \frac{\Im F}{\Re F}$ (Eq. (15)), by removing β in exchange for new Eqs. (8)–(11) which balances any nonquadrature before Eq. (15) is applied.

The advantage of quadrature-balancing the data is that now F can be expressed either in rectangular or polar coordinates, with the polar angle corresponding exactly to the fringe phase angle θ . This in turn allows us to take Fourier transforms of F or $F/|F|$ and have it properly describe phase behavior.

B. Magnitude vs intensity diagnostic

Often $I(x, y)$ varies strongly due to target features or laser speckle. If the lineout for the Lissajous only covers one half to a few cycles of phase range, then the legitimate Lissajous shape may be noncircular due to natural variations in I . This may fool the user who is trying to center this lopsided shape.

In this case it is useful to plot magnitude $|F|$ vs intensity I , and adjust the gains and offsets to maximize the linearity (allowing for any horizontal offset due to incoherent intensity contributions C_n , which contributes to I but not $|F|$). Figure 6(b) shows with simulated data how non-optimal gains cause the magnitude vs intensity plot to become nonlinear.

These magnitude vs intensity plots are linear because the cosine term in Eq. (1) is multiplied by $I(x, y)\gamma$, which sets the magnitude $|F(x, y)|$. Hence the slope of these plots is γ , for quadrature phase. For nonquadrature phase it differs from this; the obliquity transformation alters apparent average $|F|$, and hence the slope, by roughly $\sim(g_q + 1)/2$, (and more exactly 0.68 for the $g_q=0.55$ of the example data).

The magnitude vs intensity plots are also useful for traditional (time dependent) VISAR data analysis. We have written an algorithm that automatically finds the optimal push-pull gains using linearity of this plot as a quality indicator, in a feedback loop. We have observed sudden changes in the slope of this plot after a shock event, and interpret this to be consistent with the change in texture of a shocked sample, which can affect spatial coherence.

C. Repairing sparse fringe ambiguities

When the intensity of reflected light is low for a location of the image, such as due to laser speckle or target texture, then the phase will be dominated by noise. A problem that occurs for noisy 2D phase data is when the phase makes a spiral topology so that a line integral of phase around a closed path is not zero, but instead an integer number of cycles. This creates a “pole” which prevents the 2D phase unwrapping from removing all the phase ambiguities.

When these phase poles are relatively sparse, then a solution is to replace a region around the pole with substitute data which is well behaved. This could be smoothed data or a model of expected behavior.

We blurred $\theta_{orig}(x, y)$ by ~ 20 pixels to form $\theta_{blur}(x, y)$. Then we formed a linear combination of the original data with the blurred proxy using a mask function $M_{mask}(x, y)$

$$\theta_{final} = \theta_{orig} * (1 - M_{mask}) + \theta_{blur} * M_{mask}, \quad (17)$$

where M_{mask} is between 0 and 1 and indicates presence of a defect. (The M_{mask} is set by deviations of θ_{orig} from θ_{blur} that exceed some threshold, or excessive phase slopes.) These mask spots are expanded laterally by an amount similar to the blur used to form θ_{blur} . This can be done by blurring M_{mask} , then limiting its value to a fraction of its original height, say 5%. Then dividing by 0.05 so that once again its value is between 0 and 1, but now it has widened regions which have a taper at the edges. In the example shot, the density of poles is low such that M_{mask} is only a few percent of total image area.

D. Response to discontinuous features

The time response of the 2D-VISAR is the same as a traditional line—or point—VISAR. Namely, the response to a perfect step-function change in velocity is a linearly blurred transition, having a width equal to the delay ($\tau = 268.5$ ps). Now if the shock front is tilted or curved as it emerges from the target, then even though the 2D-VISAR measures only a single moment, the curvature causes a relation between time and position across the target. This means that there could be a linearly blurred edge to shock features. Such a linear edge is seen in the four edges of the driven region in Fig. 10.

If however the shock was perfectly planar as it emerges, there would be a crisp discontinuity at edge of driven region (limited by target optics blur of a few pixels).

IV. ANALYSIS ON EXAMPLE DATA

A. Spatial uniformity of gains in data

Data analysis is simplest when one can apply a single set of push-pull parameters across the entire image. This is the case for our example shot, as is confirmed by Fig. 7 which evaluates a Lissajous along a horizontal line at three locations, $Y = 700, 1000,$ and 1700 , and shows that the Lissajous is circular and centered in all three locations, using the same gains, and the magnitude vs intensity plots are linear. For example, an incorrect offset h_0 or v_0 would cause the $|F|$ vs I plot to quickly deviate from linearity for small magnitudes

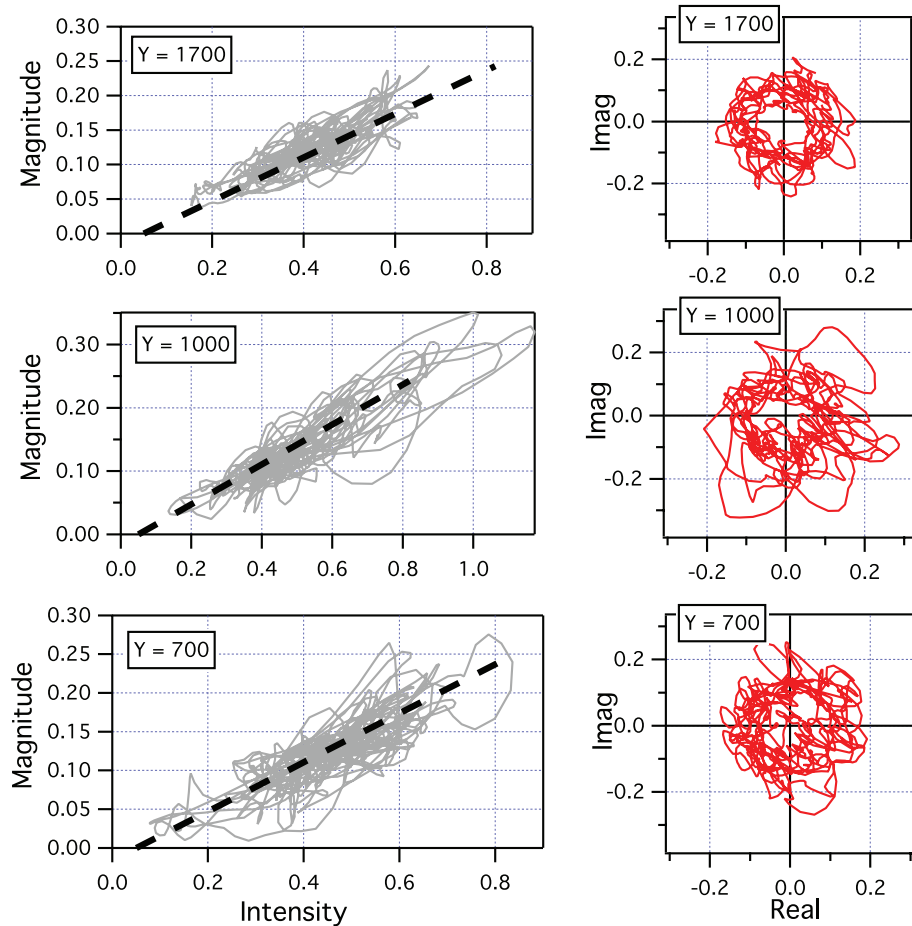


FIG. 7. Confirmation for this shot that a single choice of push-pull gain parameters works for the entire image, since the Lissajous plots (right column) remain circular and the $|F|$ vs I plots (left column) remain linear in three different locations on the image. The Lissajous describe horizontal lineouts at $Y=700$, 1000, and 1700, where X varies from 500 to 1600. The dashed line is guide for eyes, same in each plot.

where loops of the Lissajous are near the origin. Figure 8 shows that the θ produced is independent of the large fluctuations in fringe magnitude, confirming successful choice of parameters.

The slope of the magnitude vs I data is ~ 0.3 . This is consistent with theory, which says for $g_q=0.55$ of the example data the average $|F|$ is 0.68. And the maximum γ of 0.5 (due to partial coherence of the white light arrangement) times 0.68 is 0.34, which is larger than but similar to 0.3, as it should be.

B. 2D nonfringing and fringing images

The results of the push-pull analysis on the example shot are shown in Fig. 9 as ordinary nonfringing image $I(x, y)$, Fig. 10 as wrapped phase $\theta(x, y)$, and Fig. 11 as unwrapped phase. In the nonfringing image Fig. 9, the distribution of darker lines within the shocked region (slightly out of focus) is due to spatially dependent deformation at the Si-free surface interface.

The contour map appearance of the wrapped phase (Fig. 10) is useful for displaying simultaneously both sub-cycle details and gross behavior. Unwrapping it to produce Fig. 11 shows the overall plateau shape having interesting

bumps of ~ 100 pixel ($50 \mu\text{m}$) scale which appears to be related to the spatially dependent deformation response of Si.

Si and more generally strongly covalently bonded crystals are brittle at room temperature due to the slow velocity of dislocations unable to relieve an applied stress field: a tendency enhanced in Si by the typically low initial dislocation density ($< 10^8 \text{ m}^{-2}$). However in uniaxial compression experiments, as described here, inertial confinement within the bulk material is expected to suppress the onset of brittle fracture while enhancing ductility.¹⁴ At the Si free-surface, however, the conditions of inertial confinement break down and the onset of fracture is possible. The dark features observed in nonfringing image of Fig. 9 accompanied by the velocities roughness shown in Fig. 11 are consistent with the onset of fracture planes and the resulting velocity jetting.

These feature sizes lie at the spatial resolution limit of the line-VISAR; the 2D-VISAR can resolve these whereas the line-VISAR in its current mode cannot. (The 2D-VISAR records quadrature information for every pixel, whereas the line-VISAR effectively trades some of its spatial resolution to provide this quadrature information, limiting its spatial resolution to its bias fringe period, ~ 70 pixels.)

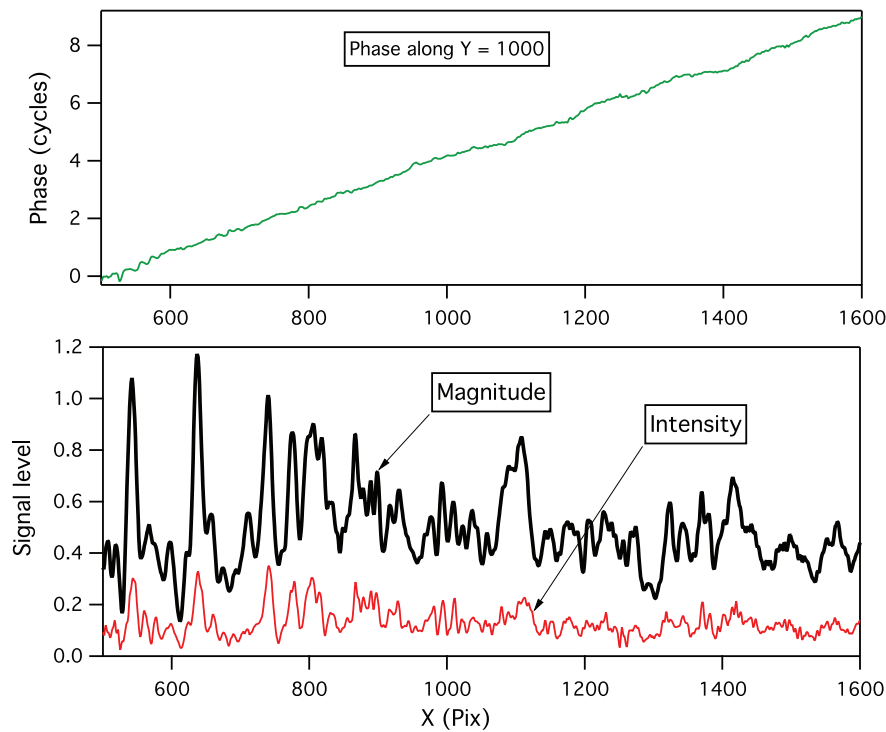


FIG. 8. In a successful push-pull analysis the phase θ variations (top) are independent of magnitude $|F|$ variations, and the magnitude and intensity I variations are similar to each other (bottom). Data from a horizontal line 10 pixels wide at $Y=1000$ for X from 500 to 1600. Bias slope in phase has not yet been removed. Bumps in phase are valid signal, not noise. The Lissajous and magnitude vs intensity plots associated with this lineout are in Fig. 7, middle.

C. Fourier analysis

Figure 12(a) shows an FFT of the 1500 pixel diameter central region of $\theta(x, y)$, apodized to taper smoothly at edges. Note the relatively increased energy in a ring at frequency

$\sim 0.01 \text{ pixel}^{-1}$. This represents the ~ 100 pixel ($55 \mu\text{m}$) scale bumps in phase map Fig. 11. The angular distribution is intriguing and consistent with $[111]$ crystal symmetry. This pattern is distinct from the FFT of $I(x, y)$ (Figure 12(b)),

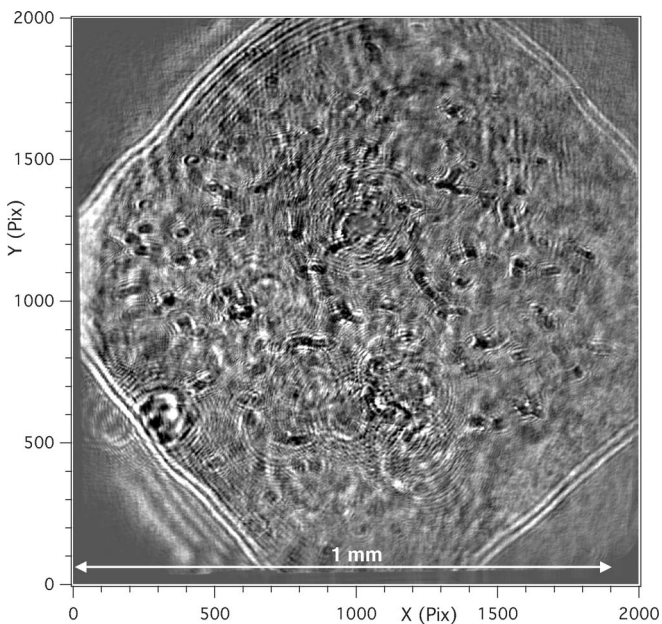


FIG. 9. The snapshot reflectivity image of target $I(x, y)$, simultaneous with phase measurement (Fig. 10), formed by summing the four quadrature images in Fig. 5 so that fringes cancel. The same was done to the reference (pre-shot) exposure and that result subtracted from the shot exposure to produce this image, to reduce artifacts contributed by dust specks on optics. The distribution of darker lines within the shocked region (slightly out of focus) is due to spatially dependent deformation at the Si-free surface interface.

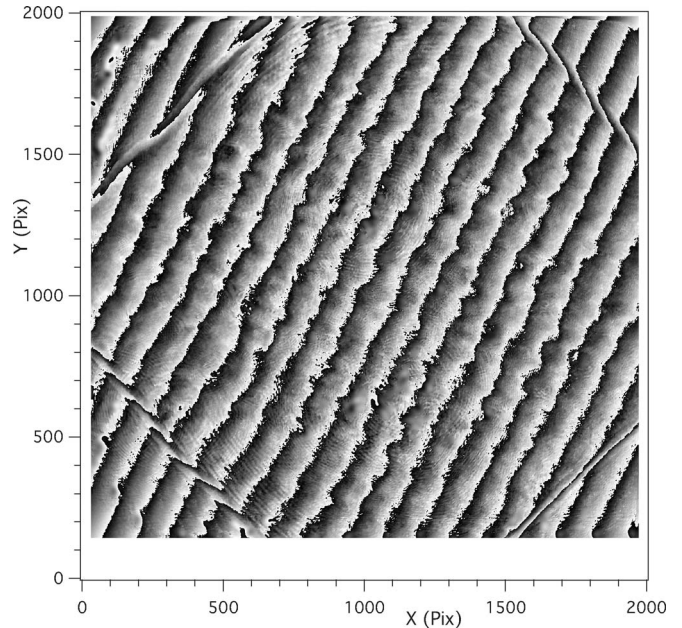


FIG. 10. Snapshot wrapped phase map $\theta(x, y)$, simultaneous to reflectivity image (Fig. 9). The phase is modulo 1 cycle, and hence the patterns can be interpolated like equi-phase contours in a topographical map. The jump of ~ 1 fringe at the four edges of the driven region, and the bumps in velocity in the central region can be clearly seen. The phase map of the pre-shot (reference) data has been subtracted to reduce artifacts due to dust specks on optics. Scale is $0.53 \mu\text{m}$ per pixel.

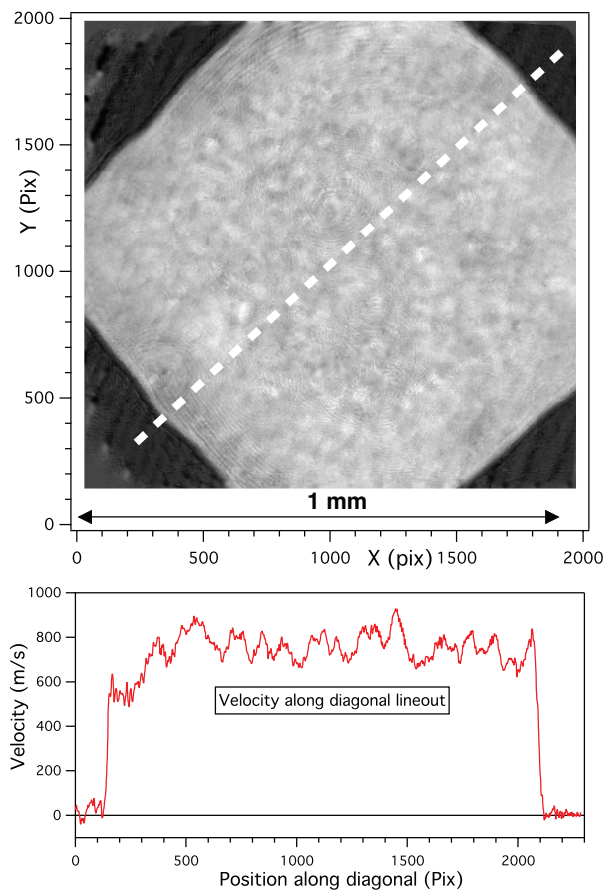


FIG. 11. (Upper) The 2D-unwrapped phase map, after the bias phase slope is removed from Fig. 10. The jump from undriven to driven region is about 1 fringe (consistent with Line-VISAR result Fig. 4). (Lower) The velocity under the 30 pixel wide dashed diagonal line from lower left to upper right. The velocity per fringe proportionality of 705 m/s per cycle was used. There are velocity bumps on a ~ 100 pixel ($\sim 50 \mu\text{m}$) scale which appears to be related to the spatially dependent deformation response of Si. These feature sizes lie at the spatial resolution limit of the line-VISAR.

demonstrating that the push-pull math successfully separates θ and I behaviors.

Figure 13 is an azimuthal average of the FFT of θ (bold curve). The FFT of the stationary target (dashed) is $\sim 10\times$ smaller, demonstrating a healthy dynamic range. The thin curve shows that the FFT of $F/|F|$ returns approximately the same result as FFT of θ . The former has the advantage of being robust to phase ambiguities that can spoil FFT of θ .

V. DISCUSSION

A. Dual VPF and multi-frame ideas

It is common practice to use dual VISAR systems having distinct VPF proportionalities observing the same target in order to reduce the ambiguity of integer fringe skips at shock events (where the fringe visibility momentarily decreases into confusion). The use of a 2nd interferometer prior to the target in the illumination beam, as in our device, does not prevent use of multiple VPFs. We are exploring several technical possibilities. We note that the VPF is proportional to the average wavelength. If the illumination consisted of two wave-

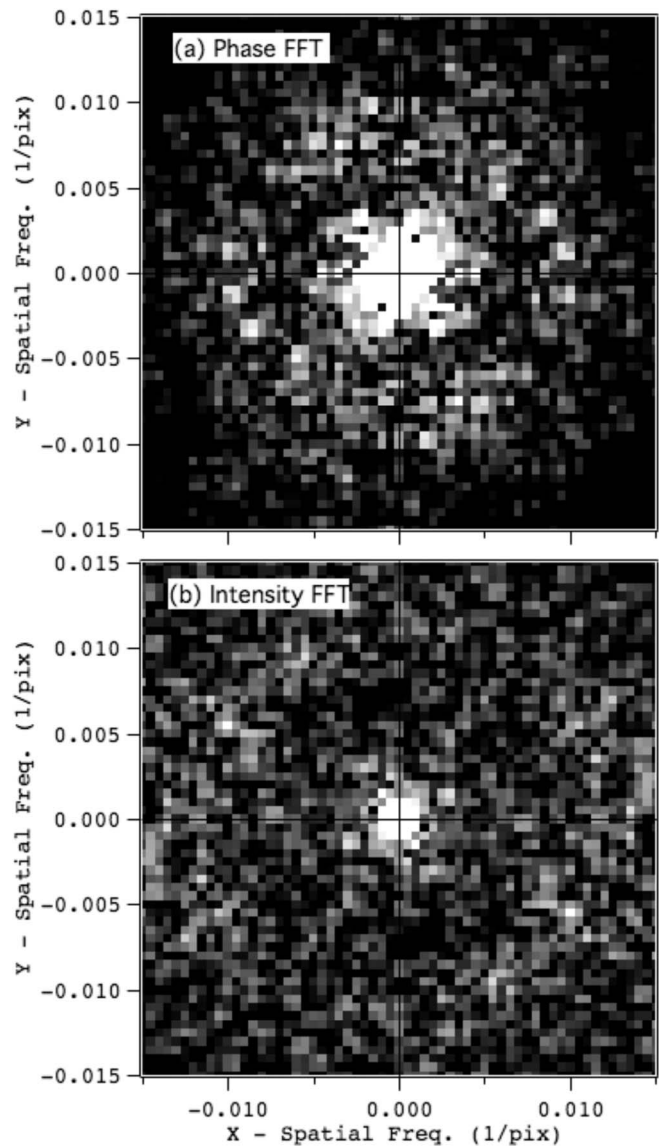


FIG. 12. (a) 2D-Fourier transform of a ~ 1500 pixel diameter apodized circular region of $\theta(x, y)$, at the center of the driven region. Phase was in radians. Grayscale shows magnitude of FFT, from 10 000 to 55 000 so that the ring-like energy distribution at ~ 0.01 per pix (which generates the bumps seen in Fig. 11) can more easily be discerned. The phase map of the reference exposure has been subtracted from this analysis. (b) The FFT of $I(x, y)$; its ring of energy has 30% higher frequency.

lengths, and a dichroic mirror was used to separate the two wavelengths to two different detectors, then two simultaneous VPFs could be used on the same target.

A multiple frame 2D-VISAR could be accomplished by wavelength encoding a series of illumination pulses arriving at different times at the target. These pass through the VISAR to a dispersive element which directs them to different positions on a detector. Note that the use of the white light arrangement means one can use incoherent illumination sources, not restricted to coherent sources of a traditional VISAR, increasing the technical options.

B. Challenging problem of dense fringe ambiguities

The technique described earlier for removing fringe ambiguities (Sec. III C) fails when the density of poles grows

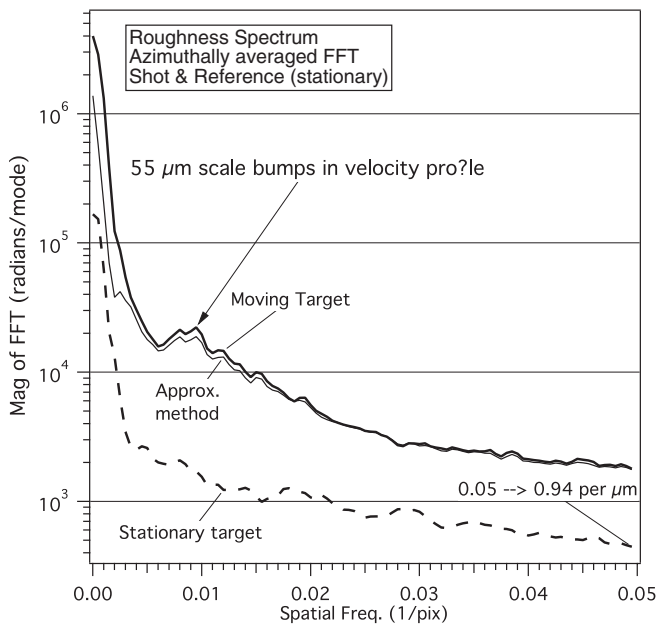


FIG. 13. Roughness spectra are the azimuthal average of the 2D-FFT of Fig. 12(a). Bold curve is FFT of θ in radians. Thin curve (approximate method) is FFT of $F/|F|$ and is robust to phase ambiguities. Dashed curve is measurement of stationary target. Bumps of 100 pixel ($\sim 55 \mu\text{m}$) scale seen in velocity profile (Fig. 11) correspond to peak at $\sim 0.01 \text{ pixel}^{-1}$.

large, since then an excessive fraction of the total image area is proxy data lacking high spatial frequency science information. Many of our 2D-VISAR shots have some regions where the phase appears chaotic and density of poles very high. We are still exploring algorithms which can properly handle such chaotic phase regions. We are also exploring improving the illumination optics to reduce laser speckle which is the cause of some of the dark noisy regions.

VI. CONCLUSIONS

We apply a push-pull data analysis to the four output images of the 2D-VISAR. The analysis is similar to conventional single-point VISAR push-pull analyses, except:

1. We balance the data as a first step, including the non-quadrature or obliquity. The balanced data allow the

complex expression of the fringes F to be in its natural form where the polar angle is exactly the same as the fringe phase. This in turn allows using F for Fourier operations, which has the advantage of being robust to phase ambiguities that can harm the FFT of θ .

2. A useful new diagnostic for judging the quality of the push-pull and quadrature balancing is the linearity of fringe magnitude $|F|$ vs intensity I . (Conventional VISAR analysis packages typically do not output this information, only θ .)
3. Fourier analysis of θ or $F/|F|$ is useful to reveal science features.
4. We observe interesting bumps in the velocity profile of spatial scale $\sim 55 \mu\text{m}$ in shocked crystalline [111] Si soon after the shock arrival.

ACKNOWLEDGMENTS

This work performed under the auspices of the U.S. Department of Energy by Lawrence Livermore National Laboratory under Contract No. DE-AC52-07NA27344. We thank the Jupiter Laser facility for their support. Thanks to Jon Eggert's continual enthusiasm and advice for novel diagnostic techniques and analysis.

¹L. Barker and R. Hollenbach, *J. Appl. Phys.* **43**, 4669 (1972).

²W. Hemsing, *Rev. Sci. Instrum.* **50**, 73 (1979).

³W. Hemsing, A. Mathews, R. Warnes, M. George, and G. Whittemore, in *Shock Compression of Condensed Matter-1991*, edited by S. Schmidt (North-Holland, 1992), pp. 767–770.

⁴D. Dolan, Sandia Report SAND2006-1950, 2006.

⁵D. Erskine and N. Holmes, *Nature (London)* **377**, 317 (1995).

⁶D. J. Erskine and N. C. Holmes, in *High Speed Photography and Photonics*, SPIE Vol. 2869, edited by D. L. Paisley (1997), pp. 1080–1083.

⁷P. M. Celliers, D. J. Erskine, C. M. Sorce, D. G. Braun, O. L. Landen, and G. W. Collins, *Rev. Sci. Instrum.* **81**, 035101 (2010).

⁸D. Erskine, U.S. patent 5,642,194 (1997).

⁹D. Erskine, U.S. patent 6,115,121 (2000).

¹⁰P. M. Celliers, D. J. Erskine, S. T. Prisbrey, D. G. Braun, J. B. Richards, C. M. Sorce, G. W. Collins, R. J. Wallace, O. L. Landen, and A. Nikroo, APS Meeting Abstract, 2007, p. 6009.

¹¹P. M. Celliers, D. J. Erskine, D. G. Braun, S. T. Prisbrey, G. W. Collins, R. J. Wallace, O. L. Landen, J. Biener, A. V. Hamza, C. Wild, E. Woerner, and A. Nikroo, APS Meeting Abstract, 2009, p. 4005.

¹²D. Ghiglia and M. Pritt, *Two Dimensional Phase Unwrapping - Theory, Algorithms and Software* (Wiley, 1998).

¹³L. Barker and K. Schuler, *J. Appl. Phys.* **45**, 3692 (1974).

¹⁴J. Tirosh and O. Abraham, *Mech. Mater.* **39**, 760 (2007).